Supplemental Information

EXTENDED DISCUSSION

Translation and Transcription Crosstalk

A defining feature of eukaryotic cells is the compartmentalization that separates translation from transcription. However, recent findings reveal that, to produce a specific set of proteins at a given time, these distinct processes are subject to robust and rapid regulation at several levels involving crosstalk between the transcription and the translation machineries, including RNA polymerase, ribosome, transcription factors, and aminoacyl-tRNA synthetases (Preker and Jensen, 2010). For example, the RBP4/ 7 subunits of RNAPII were released from nucleus to cytoplasm where it binds translation initiation factor 3 and promotes translation initiation; and ribosomal subunit S3 and L4 could interact with distinct transcription factors and regulate selective gene transcription (Egoh et al., 2010; Harel-Sharvit et al., 2010; Wan et al., 2007). Unlike the canonical processes of translation and transcription, the structural mechanisms underlying control of these coupled processes are unclear. Our data establish that the dual function of LysRS is controlled by phosphorylation through a dynamic structural switch. Ser207-phosphorylation of LysRS disrupts multiple H-bonds and creates strong steric clashes at the domain-domain interface, resulting an opening of the *N*-terminal tRNA anticodon-binding domain. This open conformer disrupts the binding pocket for the MSC p38/ AIMP2 scaffold protein and thus dissociates $LysRS^{pS207}$ from cytoplasm to

the nucleus. Moreover, this open conformer provides an efficient platform for performing novel functions. Both Ap_4A catalysis and MITF-binding sites are located in the central region of the LysRS homodimer that are exposed in the open conformer, which may coordinate production of Ap_4A with the release of Hint-1 repressor from MITF.

Exclusive Switch of LysRS from Translation to Transcription

The ability to undergo substantial conformational changes appears to be a shared feature for phosphorylation-dependent activation of signaling macromolecules, such as the common Src and CDK-like kinases (Deindl et al., 2007; Lietha et al., 2007; Sicheri et al., 1997; Xu et al., 1997). For example, phosphorylation of Src disrupts the interaction of the SH2 domain with the *C*-terminal tail of the kinase domain, thereby activating the kinase catalytic site to target downstream proteins (Xu et al., 1997; Young et al., 2001). However, due to the essentiality of aminoacylation, the closed conformation of unphosphorylated LysRS forms an active functional state essential for protein translation. In contrast to the inactive to active (ON/ OFF) switch of kinases, the conformational change of LysRS conforms to a unique bi-functional (A/ B) switch. Moreover, because transcription and translation are performed in separate compartments in eukaryotes, it is possible that LysRS simply directs its dual roles as a result of its change in localization. However, in four different ways our data demonstrated that the translational function of LysRS is terminated when it switches to its role in transcription. First, as LysRS is bound to the MSC, it is spatially retained in

this cytoplasmic reservoir and thus cannot regulate transcription in the nucleus. Second, to be released from the MSC and mobilized to the nucleus, an open conformation of $LysRS^{pS207}$ is needed to disrupt its interaction with MSC p38/ AIMP2 (Figure 3D). However, because it traps the bound tRNA away from the active site, the open conformation of $LysRS^{pS207}$ is defective for aminoacylation. Third, because Ap_4A synthesis occurs at the same active site at which Lys-AMP is transferred to tRNA, aminoacylation activity competes with Ap_4A synthesis, which is blocked when free tRNA is available (Hilderman and Ortwerth, 1987). Thus, to produce Ap_4A, phosphorylation is needed to open up the LysRS structure and to abolish its aminoacylation activity (Figure S6A). Not surprisingly, forced expression of native LysRS does not lead to increased levels of Ap_4A in mast cells when they are treated with a MAPK kinase inhibitor that prevents Ser207 phosphorylation (Yannay-Cohen et al., 2009). Finally, the interaction between LysRS and MITF, which depends on the phosphorylation of LysRS, is through the catalytic domain of LysRS and, is auto-inhibited by the *N*-terminal domain in native LysRS (Figure 6B). Therefore, phosphorylation of LysRS switches its function from exclusively translational to exclusively transcriptional.

Implication for Non-canonical Functions of LysRS in General

The observed structural changes might also be relevant for the other non-canonical roles of LysRS. In addition to being released from the cytoplasmic MSC to form a complex with nuclear MITF to drive the expression of genes that regulate the immune response,

LysRS also interacts with the HIV Gag protein and helps the packing of $tRNA^{Lys}$ into the virus as a primer for reverse transcription of the HIV genome (Kleiman et al., 2010). In addition, LysRS also functions as a cytokine that binds to macrophages and peripheral blood mononuclear cells to activate their migration and TNF-α production (Park et al., 2005). Recent work reveals that phosphorylated LysRS (at a different site) is dissociated from the MSC to bind the 67LR laminin receptor for enhancing cancer cell migration (Kim et al., 2012). Our results on $LysRS^{pS207}$ suggest that distinct structural conformations of LysRS regulated by post-translational modifications may be the key mechanism to perform these various functions.

EXTENDED EXPERIMENTAL PROCEDURES

Expression Constructs

The Human full-length LysRS (1-597) gene was previously codon-optimized and cloned in vector pBADito (Invitrogen, Grand Island, NY) with a *C*-terminal His6x-tag (Guo et al., 2008). An N-terminal Flag-tagged human full-length LysRS version was also cloned into vector pcDNA3.1 (Invitrogen) for expression in mammalian cells. A compact version of human LysRS (70-584) was constructed with a *C*-terminal His6x-tag linked by a TEV-cleavage site for SAXS analysis, or without tag into the pET20b vector for crystallization. The gene encoding human MSC p38/ AIMP2 was synthesized by codon optimization. The N-terminal human p38/ AIMP2 sequence (1-48) was cloned into vector pET28a with a *C*-terminal His6x-tag for crystallization. The N-terminal p38 sequence (1-80) was fused with *E. coli* Trbp111 (ygjh) followed by a StrepII-tag (sequence WSHPQFEK) at the *C*-terminus for pull-down experiments, and was then inserted into pET28a to generate pET28-p38$_{80}$D-StrepII. Phospho-mimetic mutation S207D and other mutations were made on both full-length LysRS and LysRS$_{70-584}$ constructs. Human MITF gene containing the basic helix-loop-helix zipper region was cloned into pET20b vector with a TEV-cleavage site linked His6x-tag. For fragment complementary assay, eGFP gene was split into two halves at position 159 (Michnick et al., 2007) and fused to the LysRS (70-584) with linkers based on structural modeling.

Protein and Complex Preparation

Human full-length LysRS, $LysRS_{70-584}$ and their mutants were expressed in the bacterial strain BL21(DE3). It was purified to homogeneity with a Ni-HiTrap affinity column (5 mL, GE Healthcare, Piscataway, NJ). To generate protein complexes, untagged pET20-LysRS was co-transformed with pET28-$p38_{48}$-His into the BL21(DE3) strain. Presence of both vectors in *E. coli* was maintained by the addition of dual antibiotics. The temperature of the bacterial culture was dropped to 16 ℃ 2 h before induction and was then induced with 0.2 mM IPTG for 20 h at 16 ℃. The cell pellet (from 4-8 liters) was lysed in low salt buffer (150 mM NaCl, 20 mM Tris-HCl pH 8.0, 15 mM imidazole), loaded onto a Ni-HiTrap column and washed with low salt buffer (150 mM NaCl, 20 mM Tris-HCl pH 8.0, 30 mM imidazole). Protein was eluted with low salt elution buffer (150 mM NaCl, 20 mM Tris-HCl pH 8.0, 250 mM imidazole). To remove free p38, the Ni-HiTrap purified LysRS / $p38_{48}$-His proteins were concentrated and then purified by gel filtration Superdex 200 column (GE Healthcare, 10/ 300 GL) with running buffer (20 mM Hepes-Na, pH 7.5, 150 mM NaCl). The peak fractions of LysRS:p38 complex were then concentrated for crystallization.

Crystallization and Structure Determination of the LysRS:p38/AIMP2 Complexes

Crystallization was done by the sitting drop method. Protein solution (30 mg/ mL) was pre-incubated with 5 mM $_L$-lysine, 5 mM AMPCPP and 10 mM $MgCl_2$ for 10 min at 4 ℃. The $LysRS_{70-584}$:$p38_{1-48}$ complex was crystallized by mixing 0.5 μL of protein solution with 0.5 μL of precipitant solution, containing 22% PEG10000, 0.1 M MES pH 6.7, and 0.1 M magnesium acetate. Crystals were collected after incubation at 18 ℃ for 3-7 days and were flash-frozen in liquid nitrogen for data collection. Data sets were obtained from

beamline LS-CAT 21-ID-F at the Advanced Photon Source (Argonne, IL). The LysRS:p38$_{1-48}$ crystal belongs to space group *P1*. Data were integrated and scaled with HKL2000 (Otwinowski and Minor, 1997). The structures were determined by molecular replacement based on the human LysRS structure (*pdb: 3BJU*) in program Molrep (CCP4, 1994). Clear electron density of p38 was seen prior to model building and refinement and the p38 model was manually built in the electron density by use of COOT (Emsley and Cowtan, 2004). After corrections for bulk solvent and overall B values, data were refined by iterative cycles of positional refinement and TLS refinement with PHENIX (Adams et al., 2010) and model building with COOT. All current models have good geometry and no residues are in the disallowed region of the Ramachandran plot. Data collection and model statistics are given in Table S1.

Small Angle X-ray Scattering (SAXS)

All SAXS data were collected at the SIBYLS beamline at an electron energy of 12 keV covering the range of momentum transfer $0.011 < S < 0.35$ Å^{-1} (Hura et al., 2009; Putnam et al., 2007). Wild-type (WT) and mutants of LysRS$_{70-584}$-TEV-His, which matched the crystal structure of human LysRS, were purified by Ni-NTA and cleaved by TEV protease to remove the C-terminal flexible His-tag. Buffer exchange was carried out by gel filtration. Proteins were loaded at concentrations of 15-20 mg/ mL, and only the peak fraction of each protein sample was used without further concentrating. All samples were isolated one day prior to data collection, flash-frozen with liquid nitrogen immediately after elution from gel filtration and stored frozen. SAXS data were collected for 3 serial dilutions of each sample at maximum of 6 and minimum 1

mg/ mL. Data were collected from two short exposures (0.5 s) and one long exposure (6 s) for each protein sample at room temperature (18-21°C). Data scaling, merging and evaluating were carried out by use of PRIMUS (Konarev et al., 2003). GNOM was used to evaluate the P(r) function (Svergun, 1992). The value of the maximum diameter of the particle, D_{max}, was determined empirically by examining the quality of the fit to the experimental data for a range of D_{max} values. *Ab initio* free atom modeling was performed with the DAMMIF program with the scattering curves as the fitting target (Franke and Svergun, 2009). 40 independent simulations were carried out for each sample. Superposition, averaging, and filtering with the DAMAVER program yielded shape reconstructions (Volkov and Svergun, 2003). These envelopes were then used as a guide to fit the crystal structures by rigid body modeling with PyMOL and Chimera (Pettersen et al., 2004).

Hydrogen/deuterium exchange (HDX) Fourier transform ion cyclotron resonance (FT-ICR) mass spectrometry

HDX methods have been described previously (Zhang et al., 2009; Zhang et al., 2008). HDX samples were prepared as for SAXS analysis. Briefly, 5 µL of sample (20 µM) was mixed with 45 µL of 20 mM Hepes, pH 7.5, and 150 mM NaCl in D_2O to initiate each HDX reaction. HDX incubation periods were 0.5, 1, 2, 4, 8, 15, 30, 60, 120 and 240 min, each followed by simultaneous quench and proteolysis (Zhang et al., 2010). HDX was quenched by 1:1 (vol/ vol) addition of protease type XIII solution in 1.0% formic acid to reduce the pH to ~2.3 and to initiate the 2 min proteolysis. The digested peptide fragments were separated by a fast LC gradient through a ProZap C_{18} column (Grace

Davison, 1.5 □m, 500 Å, 2.1 x 10 mm) to minimize back exchange (Zhang et al., 2009). A post-column splitter reduced the LC eluent flow rate to ~400-500 nL/ min for efficient microelectrospray ionization (micro-ESI). Microelectrosprayed HDX samples were directed to a custom-built hybrid linear quadrupole ion trap 14.5 tesla FT-ICR mass spectrometer (ThermoFisher, San Jose, CA) (Schaub et al., 2008). The total data acquisition period for each sample was 6 min. Each experiment was performed in triplicate. Data were analyzed by an in-house analysis package (Kazazic et al., 2010). Time-course deuterium incorporation levels were generated by an MEM fitting method (Zhang et al., 1997).

Aminoacylation Assay

The gene for human $tRNA^{Lys3}$ was cloned into pUC18 with T7 promoter and over-expressed in *E. coli* BL21(DE3). The tRNA was purified by phenol extraction followed by chromatography on a DEAE column. The quantity of $tRNA^{Lys3}$ was determined by the charging plateau by use of saturating LysRS. The final purity was ~70-85% as quantified by uv absorbance measurements at 260 nm (1.6 pmol/ A260). LysRS proteins were quantified by mass with the Bradford protein assay (Bio-Rad, Hercules, CA). Aminoacylation was performed at 37 °C in an assay buffer (50 mM HEPES, pH 7.5, 20 mM KCl, 10 mM $MgCl_2$, 2 mM DTT, 0.003 U/ mL dialyzed yeast inorganic pyrophosphatase) with ATP (2 mM) and human $tRNA^{Lys3}$ (8 μM). Lysine charging was done in the presence of LysRS WT or mutants and [3H]-L-Lys (100 μM). Aliquots were quenched at different time intervals and precipitated in 96-well Multiscreen filter plates

(Millipore) as described previously (Beebe et al., 2007). After washing and elution by 0.2 M NaOH, samples were counted in a MicroBeta plate reader (PerkinElmer).

Ap_4A Synthesis Assay

The Ap_4A synthesis activity was analyzed by phosphoimaging (Molecular Imager FX, Biorad, Hercules, CA) with 5 mM α-32P-ATP and 0.5 μM of the purified LysRS WT, LysRS_S207D protein. The mixtures were incubated at 37 °Cin buffer containing 50 mM Hepes pH 7.5, 20 mM KCl, 10 mM $MgCl_2$, 0.25 mM L-lysine, 150 μM $ZnCl_2$ and 0.03 U/ mL dialyzed yeast inorganic pyrophosphatase. Aliquots were quenched at different time intervals by 0.5 N HCl and 50 mM EDTA, followed by phenol extraction. The aqueous phase from each sample was loaded onto methanol-dried TLC plate (PEI Cellulose F Glass, Merck, Germany), developed for 45 min in solution containing 3 M ammonium sulfate, 2% Na-EDTA, pH5.5, and dried prior to quantification.

ATP-Hydrolysis Assay

ATP hydrolysis was performed at 37 °Cin an assay buffer (50 mM HEPES, pH 7.5, 20 mM KCl, 10 mM $MgCl_2$, 2 mM DTT, 1 mM L-lysine, 0.003 U/ mL dialyzed yeast inorganic pyrophosphatase) with γ-32P-ATP (250 μM) and LysRS (1.25 μM). Aliquots were quenched at different time points in 96-well Multiscreen filter plates (Millipore) containing 8% charcoal and 1.4% $HClO_4$ as described previously (Beebe et al., 2007). After spinning the hydrolyzed phosphate into a collection plate, samples were counted in a MicroBeta plate reader (PerkinElmer, Waltham, MA).

Electrophoretic Mobility Shift Assay

Transfer RNA^{Lys3}-binding reactions for electrophoretic mobility shift assays (EMSAs) were carried out with the full-length LysRS WT, S207D, G540Y mutants. Various concentrations of the proteins (0, 0.1, 0.2 to 7.5 μM) and 3'-32P labeled human $tRNA^{Lys3}$ (100 nM) were used in 20 mM HEPES (pH 7.5), 20 mM KCl, 5 mM MgCl2, and 2 mM DTT. The mixture was incubated on ice for 10 min in a total volume of 10 uL. The 32P-labeled $tRNA^{Lys3}$ was resolved by electrophoresis on a step gradient native acrylamide gel (10%) in ½ TB buffer, visualized by exposure to phosphoimager and scanning by Molecular Imager FX (Biorad, Hercules, CA).

Isothermal Titration Calorimetry (ITC)

ITC experiments were performed at 298K with a Nano-ITC unit (TA Instruments, New Castle, DE) in 20 mM Hepes pH 7.5 and 200 mM NaCl. Human LysRSproteins (WT, S207D, LysRS-$C_{220-548}$, LysRS-N_{70-219}, and LysRS-N_{70-219}-S207D) were injected in 25 injections of 2 μL each to MITF b-HLH-Zip domain (residues 200-297) in the ITC cell (0.038 mM, 0.162 mL). Background heat of the dilution of LysRS proteins into buffer alone was subtracted and titration curve was fitted by the Nanoanalyze program (TA Instruments, New Castle, DE).

eGFP Protein Fragment Complementation Assay

$eGFP_N$-LysRS-$eGFP_C$ constructs or empty pIRESpuro vector (2.5 μg) were transfected into 6-well plates of Hek293T17 cells at ~90% confluence for 48 h. Within the wells were coverslips (Fisher Scientific) pretreated with 10 μg/ mL of collagen IV (Sigma-Aldrich Corp. St. Louis, MO) in 0.01 M acetic acid containing 5 mM $CaCl_2$ and 5 mM $MgCl_2$ for

24 h for optimum cell adherence. The cells were then fixed in ice-cold 3.5% paraformaldehyde solution for 15 min and then rinsed and stained with DAPI (1:10,000, Anaspec, Fremont, CA) for 5 min and mounted to Superfrost Plus microscope slides (Fisher Scientific) by use of Shurmount water-based mounting media (Electron Microscopy Sciences). The slides were then imaged with a Zeiss LSM 780 confocal microscope and quantified by use of image J.

Yeast Viability Assay

The cDNA sequences encoding full length human LysRS and its mutations were constructed in the p413-GAL1 vector multi-cloning site. The plasmids were then transformed into the yTHC mutant strain obtained from Open Biosystems (Lafayette, CO) according to the LiAc/ ssDNA/ PEG method (Gietz and Woods, 2002). yTHC was provided in the haploid strain R1158 background (URA:: CMV-tTA MATa his3-1 leu2-0 met15-0). The endogenous promoter of yeast cytoplasmic LysRS gene (*krs1*) has been replaced with a TET-titratable promoter in the yTHC genome. Thus, the expression of the gene can be switched off by the addition of doxycycline to the yeast's growth medium (Mnaimneh et al., 2004). Tenfold serial dilutions of freshly grown yeast cells were spotted onto selective media SCM-HIS (synthetic complete medium without histodine) containing 1% galactose and 2% raffinose (with or without doxycycline). Plates were incubated at 30°C for 3 days and then photographed.

Cell Culture

RBL-2H3 cells were maintained in RPMI 1640 medium as previously described [57]. Leukemia (RBL) cells were sensitized first with anti-DNP IgE monoclonal antibody (SPE-7; Sigma-Aldrich Corp., St. Louis, MO) and then challenged with DNP (Sigma-Aldrich Corp.). IgE antibody was centrifuged (18,000 g, 5 min) before use to remove aggregates. Cell activation was verified by demonstrating an increased phosphorylation of extracellular signal-regulated kinase (ERK) following the antigen challenge.

Gel Electrophoresis and Western Blot

Protein concentration was determined with a Tecan microplate reader (Tecan, Research Triangle Park, NC). Equal amounts of protein from each sample were resolved by either 10% or 15% SDS-PAGE under reducing conditions and transferred to polyvinylidene difluoride (PVDF) membranes. Visualization of reactive proteins was performed by enhanced chemiluminescence.

Immunoprecipitation

The immunopercepitation from RBL cells was performed as previously described (Levy et al., 2002). Immunoprecipitations in HEK293T cells were performed with a Thermo co-immunoprecipitation kit (26149) according to the manufacturer's instructions. Briefly, 10 µg of mouse M2 anti-FLAG antibody was immobilized onto AminoLink plus coupling resin for each transfection. Hek293T17 cells (ATCC), were grown to ~90% confluence and transfected with 15 µg of each FLAG-tagged LysRS WT or mutants with Lipofectamine 2000. After 24 h, the cell lysates were added to the resin at 4 ^{o}C for approximately 12 h. The resin was washed and the protein complexes eluted and

mixed with NuPage LDS loading buffer (Invitrogen) containing 0.1 M DTT. The eluents (and whole cell lysates) were run on 4-12% Tris/ Glycine NuPage gels and wet transferred to 0.45 µm PVDF membranes (Millipore). After blocking for 1 h in 5% milk in TBST (Tris-buffered saline with Tween 20), the membranes were exposed to the following primary antibodies overnight: anti-LysRS (1:1000, Santa Cruz Biotech), anti-p38/ AIMP2 (1:1000, Abcam), anti-p18/ AIMP1 (1:1000, Abcam), anti-ProRS (1:1000, Santa Cruz Biotech), anti-IleRS (1:1000, Santa Cruz Biotech), anti-MetRS (1:1000 Santa Cruz Biotech), and normalized to anti-β Tubulin (1:10,000, Thermo Scientific). Secondary HRP conjugated anibodies (goat-anti-mouse and goat-anti-rabbit 1:5000, Jackson Immunoresearch) were applied for 2 h, the membranes were immersed briefly in SuperSignal West Pico Chemiluminescent Substrate (Thermo Scientific) and exposed to film and developed on Axomat 2000 processor (Kodak).

Transfection

Amaxa Nucleofector technology (Amaxa, Cologne, Germany) was used to transfect RBL cells. A total of 2×10^6 cells were transfected with 3 µg of the selected DNA plasmid or siRNA oligonucleotide according to the manufacturer's protocol. The cells were resuspended in 100 µL Ingenio solution (Mirus, WI), either DNA (plasmid) or RNA was added, and the mixture was transferred to an electroporation cuvette. Electroporation was performed with the T-20 program.

Immunohistochemistry

RBL cells were grown on glass coverslips in 6-well plates. After extensive washing with PBS, the cells were fixed with 1.5 mL 4% formaldehyde in PBS for 10 min. The fixed cells were then washed with PBS and permeabilized with 1.5 ml Triton 1003 diluted 1:2 with PBS containing 7.5 mg bovine serum albumin. After 1 h blocking with 5% BSA, the cells were stained with rabbit anti-LysRS and followed by the addition of Cy5-conjugated goat anti-rabbit IgG and mouse anti MITF followed by the addition of Cy3-conjugated goat anti-mouse IgG (Jackson ImmunoResearch Inc., West Grove, PA). Fluorescence analysis was performed with a Zeiss LSM 410 confocal laser scanning system connected to a Zeiss Axiovert 135M microscope (Zeiss, Germany).

ImageStream Flow Cytometry

An ImageStream instrument automatically acquires up to six different spatially registered images (bright-field, dark-field, and four fluorescent images) per cell at rates on the order of thousands of objects per minute, with a digital charge-coupled device (CCD) camera. The digital imagery obtained is analyzed with the IDEAS statistical image analysis program, which provides tools for the objective numerical scoring and discrimination of cells based on the characteristics of their imagery. The ability to numerically score large numbers of automatically acquired images is ideally suited to the analysis of nuclear translocation within primary immune system cells.

Confocal Live Imaging

Live imaging was produced by Zeiss LSM confocal microscopy. The images were processed by a ZEN image browser. The cells were transfected with eGFP-LysRS or

eGFP-LysRS S207D. 24 hours after the transfection, the RBL cells were triggered with IgE-DNP, images were taken every 30 seconds as each frame.

SUPPLEMENTAL REFERENCES

Adams, P.D., Afonine, P.V., Bunkoczi, G., Chen, V.B., Davis, I.W., Echols, N., Headd, J.J., Hung, L.W., Kapral, G.J., Grosse-Kunstleve, R.W., *et al.* (2010). PHENIX: a comprehensive Python-based system for macromolecular structure solution. Acta Crystallogr D Biol Crystallogr *66*, 213-221.

Beebe, K., Waas, W., Druzina, Z., Guo, M., and Schimmel, P. (2007). A universal plate format for increased throughput of assays that monitor multiple aminoacyl transfer RNA synthetase activities. Analytical biochemistry *368*, 111-121.

CCP4 (1994). The CCP4 suite: programs for protein crystallography. Acta Crystallogr D Biol Crystallogr *50*, 760-763.

Deindl, S., Kadlecek, T.A., Brdicka, T., Cao, X., Weiss, A., and Kuriyan, J. (2007). Structural basis for the inhibition of tyrosine kinase activity of ZAP-70. Cell *129*, 735-746.

Egoh, A., Nosuke Kanesashi, S., Kanei-Ishii, C., Nomura, T., and Ishii, S. (2010). Ribosomal protein L4 positively regulates activity of a c-myb proto-oncogene product. Genes Cells *15*, 829-841.

Emsley, P., and Cowtan, K. (2004). Coot: model-building tools for molecular graphics. Acta Crystallogr D Biol Crystallogr *60*, 2126-2132.

Franke, D., and Svergun, D. (2009). DAMMIF, a program for rapid ab-initio shape determination in small-angle scattering. J Appl Cryst *42*, 342-246.

Gietz, R.D., and Woods, R.A. (2002). Transformation of yeast by lithium acetate/ single-stranded carrier DNA/ polyethylene glycol method. Methods Enzymol *350*, 87-96.

Goerlich, O., Foeckler, R., and Holler, E. (1982). Mechanism of synthesis of adenosine(5')tetraphospho(5')adenosine (AppppA) by aminoacyl-tRNA synthetases. Eur. J. Biochem. *126*, 135-142.

Guo, M., Ignatov, M., Musier-Forsyth, K., Schimmel, P., and Yang, X.L. (2008). Crystal structure of tetrameric form of human lysyl-tRNA synthetase: Implications for multisynthetase complex formation. Proc Natl Acad Sci U S A *105*, 2331-2336.

Harel-Sharvit, L., Eldad, N., Haimovich, G., Barkai, O., Duek, L., and Choder, M. (2010). RNA polymerase II subunits link transcription and mRNA decay to translation. Cell *143*, 552-563.

Hilderman, R.H., and Ortwerth, B.J. (1987). A preferential role for lysyl-tRNA4 in the synthesis of diadenosine 5',5'''-P1,P4-tetraphosphate by an arginyl-tRNA synthetase-lysyl-tRNA synthetase complex from rat liver. Biochemistry *26*, 1586-1591.

Hura, G.L., Menon, A.L., Hammel, M., Rambo, R.P., Poole, F.L., 2nd, Tsutakawa, S.E., Jenney, F.E., Jr., Classen, S., Frankel, K.A., Hopkins, R.C., *et al.* (2009). Robust, high-throughput solution structural analyses by small angle X-ray scattering (SAXS). Nat Methods *6*, 606-612.

Kazazic, S., Zhang, H.M., Schaub, T.M., Emmett, M.R., Hendrickson, C.L., Blakney, G.T., and Marshall, A.G. (2010). Automated data reduction for hydrogen/ deuterium exchange experiments, enabled by high-resolution Fourier transform ion cyclotron resonance mass spectrometry. J Am Soc Mass Spectrom *21*, 550-558.

Kim, D.G., Choi, J.W., Lee, J.Y., Kim, H., Oh, Y.S., Lee, J.W., Tak, Y.K., Song, J.M., Razin, E., Yun, S.H., *et al.* (2012). Interaction of two translational components, lysyl-tRNA

synthetase and p40/ 37LRP, in plasma membrane promotes laminin-dependent cell migration. FASEB journal : official publication of the Federation of American Societies for Experimental Biology.

Kleiman, L., Jones, C.P., and Musier-Forsyth, K. (2010). Formation of the tRNALys packaging complex in HIV-1. FEBS Lett. *584*, 359-365.

Konarev, P.V., Volkov, V.V., Sokolova, A.V., Koch, M.H.J., and Svergun, D.I. (2003). PRIMUS - a Windows-PC based system for small-angle scattering data analysis. J Appl Cryst *36*, 1277-1282.

Levy, C., Nechushtan, H., and Razin, E. (2002). A new role for the STAT3 inhibitor, PIAS3: a repressor of microphthalmia transcription factor. J. Biol. Chem. *277*, 1962-1966.

Lietha, D., Cai, X., Ceccarelli, D.F., Li, Y., Schaller, M.D., and Eck, M.J. (2007). Structural basis for the autoinhibition of focal adhesion kinase. Cell *129*, 1177-1187.

Michnick, S.W., Ear, P.H., Manderson, E.N., Remy, I., and Stefan, E. (2007). Universal strategies in research and drug discovery based on protein-fragment complementation assays. Nature reviews. Drug discovery *6*, 569-582.

Mnaimneh, S., Davierwala, A.P., Haynes, J., Moffat, J., Peng, W.T., Zhang, W., Yang, X., Pootoolal, J., Chua, G., Lopez, A., *et al.* (2004). Exploration of essential gene functions via titratable promoter alleles. Cell *118*, 31-44.

Otwinowski, Z., and Minor, W. (1997). Processing of X-ray diffraction data collected in oscillation mode. Methods in Enzymology *276*, 307-326.

Park, S.G., Kim, H.J., Min, Y.H., Choi, E.C., Shin, Y.K., Park, B.J., Lee, S.W., and Kim, S. (2005). Human lysyl-tRNA synthetase is secreted to trigger proinflammatory response. Proc Natl Acad Sci U S A *102*, 6356-6361.

Pettersen, E.F., Goddard, T.D., Huang, C.C., Couch, G.S., Greenblatt, D.M., Meng, E.C., and Ferrin, T.E. (2004). UCSF Chimera--a visualization system for exploratory research and analysis. J Comput Chem *25*, 1605-1612.

Preker, P., and Jensen, T.H. (2010). Translation by remote control. Cell *143*, 501-502.

Putnam, C.D., Hammel, M., Hura, G.L., and Tainer, J.A. (2007). X-ray solution scattering (SAXS) combined with crystallography and computation: defining accurate macromolecular structures, conformations and assemblies in solution. Q Rev Biophys *40*, 191-285.

Schaub, T.M., Hendrickson, C.L., Horning, S., Quinn, J.P., Senko, M.W., and Marshall, A.G. (2008). High-performance mass spectrometry: Fourier transform ion cyclotron resonance at 14.5 Tesla. Anal Chem *80*, 3985-3990.

Sicheri, F., Moarefi, I., and Kuriyan, J. (1997). Crystal structure of the Src family tyrosine kinase Hck. Nature *385*, 602-609.

Svergun, D. (1992). Determination of the Regularization Parameter in Indirect-Transform Methods Using Perceptual Criteria. J Appl Cryst *25*, 495-503.

Volkov, V.V., and Svergun, D. (2003). Uniqueness of ab-initio shape determination in small-angle scattering. J Appl Cryst *36*, 860-864.

Wan, F., Anderson, D.E., Barnitz, R.A., Snow, A., Bidere, N., Zheng, L., Hegde, V., Lam, L.T., Staudt, L.M., Levens, D., *et al.* (2007). Ribosomal protein S3: a KH domain subunit in NF-kappaB complexes that mediates selective gene regulation. Cell *131*, 927-939.

Xu, W., Harrison, S.C., and Eck, M.J. (1997). Three-dimensional structure of the tyrosine kinase c-Src. Nature *385*, 595-602.

Yannay-Cohen, N., Carmi-Levy, I., Kay, G., Yang, C.M., Han, J.M., Kemeny, D.M., Kim, S., Nechushtan, H., and Razin, E. (2009). LysRS serves as a key signaling molecule in the immune response by regulating gene expression. Mol. Cell *34*, 603-611.

Young, M.A., Gonfloni, S., Superti-Furga, G., Roux, B., and Kuriyan, J. (2001). Dynamic coupling between the SH2 and SH3 domains of c-Src and Hck underlies their inactivation by C-terminal tyrosine phosphorylation. Cell *105*, 115-126.

Zhang, H.M., Bou-Assaf, G.M., Emmett, M.R., and Marshall, A.G. (2009). Fast reversed-phase liquid chromatography to reduce back exchange and increase throughput in H/ D exchange monitored by FT-ICR mass spectrometry. J Am Soc Mass Spectrom *20*, 520-524.

Zhang, H.M., Kazazic, S., Schaub, T.M., Tipton, J.D., Emmett, M.R., and Marshall, A.G. (2008). Enhanced digestion efficiency, peptide ionization efficiency, and sequence resolution for protein hydrogen/ deuterium exchange monitored by Fourier transform ion cyclotron resonance mass spectrometry. Anal Chem *80*, 9034-9041.

Zhang, H.M., McLoughlin, S.M., Frausto, S.D., Tang, H., Emmett, M.R., and Marshall, A.G. (2010). Simultaneous reduction and digestion of proteins with disulfide bonds for

hydrogen/ deuterium exchange monitored by mass spectrometry. Anal Chem *82*, 1450-1454.

Zhang, Z., Li, W., Logan, T.M., Li, M., and Marshall, A.G. (1997). Human recombinant [C22A] FK506-binding protein amide hydrogen exchange rates from mass spectrometry match and extend those from NMR. Protein Sci. *6*, 2203-2217.

SUPPLEMENTAL FIGURE LEGENDS

Figure S1. Crystal packing of LysRS:p38/AIMP2 complexes, Related to Figure 1

(A) Experimental electron density (contoured at 1.0 σ and colored blue/ yellow for LysRS and orange for p38) superimposed with a ribbon representation of the human LysRS:p38/ AIMP21-48 complex (gray).

(B) Molecules in the LysRS:p38/ AIMP21-48 crystal lattice (2.86 Å resolution) viewed perpendicular to the b - c plane. Four LysRS dimers (8 chains) and four p38/ AIMP21-48 were found in one asymmetric unit. The N-terminal 31 residues of the p38/ AIMP21-48 (shown in black) bind to one LysRS dimer. The remaining p38/ AIMP2 residues (32-48) extended into the solvent channel and became disordered.

Figure S2. HDX-MS Mapping of human LysRS, Related to Figure 2

(A) Degree of increased deuterium incorporation for the phospho-mimetic S207D relative to WT, mapped along the sequence of LysRS.

(B) Time-course deuterium uptake plots for representative peptide segments. Each reported deteurium uptake increase was calculated from the difference in area (under the curve) between deuterium uptake vs. time profiles for the LysRS_S207D and WT. Segments with increased deuterium uptake in LysRS_S207D were mapped onto the LysRS structure and found to be at the domain-domain interface (Figure 3C). Importantly, few peptides were found with decreased deuterium uptake in

LysRS_S207D, indicating that phosphorylation of Ser207 mainly increases solvent access to LysRS.

Figure S3. SAXS Analysis of human LysRS phospho-mimetic S207D versus WT, Related to Figure 2

(A, B) Experimental small-angle X-ray scattering (SAXS) profile of human $LysRS_{70-584}$ WT (red) and phospho-mimetic S207D (blue). Theoretical scattering profile calculated from the *ab initio* model with the lowest χ value is shown for the S207D (black line). The inset shows Guinier plots (including linear fits) for the low-angle region ($S_{max} \times R_g < 1.3$) indicating no aggregation in the samples.

(C) P(r) plots from SAXS profile were calculated by the program GNOM (Svergun, J. Appl. Cryst. 1992) for the LysRS WT and S207D. The radius of gyration (R_g) increased from 38.8 ± 0.2 Å to 40.6 ± 0.3 Å and the maximum diameter (Dmax) increased from 160 Å to 195 Å in the transition of WT to the phospho-mimetic S207D.

(D, E) SAXS-based shape reconstruction of the LysRS_WT (red) and S207D (cyan) in solution. The crystal structure of dimeric LysRS was docked into the envelopes manually. Three orthogonal views are shown. Structural modeling indicates that the extended shape of LysRS_S207D corresponds to the flipped-out tRNA anticodon-binding domains to an "open" conformation (see Figure 2E).

(F) Integration of HDX-MS and SAXS results highlights the open conformation of LysRS caused by the phosphorylation of Ser207. The exposed surface in the SAXS-based structure model of $LysRS^{S207D}$ (vs. $LysRS^{WT}$) largely overlaps with the exposed surface identified in the HDX-MS analysis (orange). This result highlights the open conformation that is caused by the phosphorylation of Ser207.

Figure S4. The Open Conformer Dissociates LysRS from the MSC, Related to Figure 3

(A) Experimental small-angle X-ray scattering (SAXS) profile of human $LysRS_{70-584}$ G540Y (gray) with its theoretical scattering profile calculated from the ab initio model with the lowest χ value shown (black line).

(B) SAXS-based shape reconstruction of the $LysRS^{WT}$ (red) and $LysRSG^{540Y}$ (gray) in solution. The extended shape of $LysRS^{G540Y}$ corresponds to the flipped-out tRNA anticodon-binding domains to an open conformation, caused by the steric clash of the tyrosine side chain at position 540. The maximum diameter of $LysRS^{G540Y}$ in solution (Dmax = 200 Å) is slightly larger than that of $LysRS^{S207D}$ (Dmax = 195 Å), and 40 Å larger than LysRSWT (Dmax = 160 Å), indicating that G540Y has opened the structure to a greater extent, thus representing a pure structural opening mutant of LysRS.

(C-D) Disruption of LysRS:p38/ AIMP2 interaction by the open conformer. Mutation of G540Y or phosphor-mimetic S207D loses the interaction with endogenous MSC in cells, supporting that the disruption of the hydrophobic groove for p38/ AIMP2 by opening

up the domain-domain interface is the ultimate cause for releasing LysRS^{pS207} from the MSC. In fact, changes on either side of the interface (V101W/ D/ R, R314A, G540Y/ R, G540Y+S207D) can efficiently dissociate LysRS from the MSC.

(E) Confocal immunofluorescence microscopy showing the nuclear location of the endogenous LysRS and MITF in RBL cells at quiescent state and after IgE-DNP trigger. The red signal corresponds to LysRS staining, whereas the green corresponds to MITF staining and the blue is for nuclear DAPI. The pictures was taken by confocal microscopy in Z-mode. A representative experiment of four is shown.

Figure S5. The Open Conformer Switches off the Aminoacylation Function of LysRS but Remains its tRNA^{Lys}-binding Ability, Related to Figure 5

(A, C) Aminoacylation assays show that mutations with a bulky side chain at the dimer interface abolish tRNA charging (S207Y/ E, G540D/ E/ R/ Y/ W). Mutations with positive charge (S207R) are less effective at inhibiting aminoacylation activity, suggesting that the negative charge of the phosphate group on LysRS_Ser207 is also important for introducing repulsion between the domain interfaces. LysRS$_{70-584}$ constructs (0.5 μM) used for SAXS analysis were used in these assays. WT and mutants of S207 or G540 (on the opposite side) were analyzed with 80 μM total tRNA^{Lys3} to ensure sufficient substrate for charging.

(B) A detailed view of the domain-domain interface of LysRS structure shows that Ser207 is located at a critical position for disrupting the aminoacylation activity of human LysRS.

(D) Electrophoretic mobility shift assay showing that the LysRS_G540Y has $tRNA^{Lys3}$ binding affinity is similar to those for LysRS_WT and S207D. The following protein concentrations (0, 0.1, 0.2, 0.4, 0.8, 1.6, 2.4, 3.2, 5.0, 6.25, and 7.5 μM, respectively) were used.

Figure S6. Interaction Between LysRS and MITF Depends on Ser207 Phosphorylation, Related to Figure 6

(A) Mechanism for the Enzymatic Switch of LysRS. Transfer RNAs bind to LysRS mainly by anchoring their anticodon stem-loop onto the N-domain of LysRS. Through that anchoring, the 3'-acceptor end of the L-shaped tRNA is placed at the active site in C-domain of LysRS, where lysine is transferred from Lys-AMP to tRNA (left model). On the other hand, LysRS catalyzes Ap_4A synthesis by conjugating Lys-AMP (the adenylate intermediate product for aminoacylation) with the second bound ATP and simultaneously releases lysine (Goerlich et al., 1982). In native LysRS, because Ap_4A synthesis happens at the same active site where Lys-AMP is transferred to tRNA, Ap_4A synthesis is blocked when free tRNA is available (Hilderman and Ortwerth, 1987). Because the N-domain of $LysRS^{S207D}$ moves away from the C-domain, $LysRS^{S207D}$ traps tRNA in a nonfunctional position and allows the production of Ap_4A (right model). Not

surprisingly, because of the retention of the aminoacylation activity that competes with Ap_4A synthesis, over-expression of native LysRS did not increase Ap_4A in mast cells when phosphorylation was inhibited by a MAPK kinase inhibitor (Yannay-Cohen et al., 2009). Thus, in order to produce Ap_4A efficiently in cells, phosphorylation is needed to open up the LysRS structure and abolish its aminoacylation activity. The ramifications of that structural opening turn out to be even more profound (see main text).

(B) Co-immunoprecipitation of endogenous LysRS with MITF before and 5min after mast cell activation.

(C-E) Isothermal titration calorimetry assays for binding of the MITF bHLH-Zip domain to $LysRS^{WT}$, $LysRS^{S207D}$ or the C-terminal aminoacylation domain of LysRS.

(F-G) Isothermal titration calorimetry assay of the *N*-domains of $LysRS^{WT}$ and $LysRS^{S207D}$ fragments binding to MITF. Although the *C*-terminal aminoacylation domain binds to MITF with an affinity similar to that for full length $LysRS^{S207D}$, the *N*-terminal tRNA anticodon-binding domain of LysRS (or of $LysRS^{S207D}$) does not interact with MITF. Thus, the *N*-domain acts as a self-inhibitor that blocks the interaction of *C*-domain with MITF in $LysRS^{WT}$.

Supplementary Movie.

Movie S1: Opening Transition of the Anticodon-binding Domain of Human LysRS upon Phosphorylation, Related to Figure 2

Side view of a transition of the LysRS N-domain upon Ser207 phosphorylation is depicted. The movie shows the movement of anticodon-binding domain, which is caused by the steric clashes of phosphate group at Ser207. The domains of LysRS are colored as in Figure 3A. The intermediate states for the supplemental movies were generated with LSQMAN and illustrated with Pymol and Quicktime.

Movie S2: Bottom View of a Transition of the Anticodon-binding Domain of Human LysRS upon Phosphorylation to release p38/AIMP2, Related to Figure 6

The movie shows the bottom view of a transition of the LysRS N-domain upon Ser207 phosphorylation. These conformational changes accompany the disruption of MSC p38/ AIMP2 binding sites and the dissociation of LysRS from the MSC reservoir. In addition, these conformational changes also facilitate the subsequent Ap_4A production by the inactivation of tRNA charging and, promote the interaction with MITF through the exposed C-domain: N-domain interface.

Table S1 Summary of Crystallographic Data and Refinement Statistics of the human LysRS:p38/AIMP2 complex, related to Figure 1.

		LysRS : p38/AIMP2$_{1-48}$
Data collection		
Space group		*P1*
Cell dimensions		
	a, *b*, *c* [Å]	79.20, 122.01, 149.20
	α, β, γ [°]	89.16, 85.58, 89.71
Resolution [Å]		50.00-2.86 (2.96-2.86)[a]
R_{sym} or R_{merge} [%][b]		10.2 (48.7)
I / σI		13.3 (2.7)
Completeness [%]		99.1 (98.6)
Redundancy		4.0 (4.0)
Refinement		
Resolution [Å]		50-2.86 (2.88-2.86)
No. reflections		128750
R_{work}[c] / R_{free}[d] [%]		18.5/22.3
No. atoms		
	Protein	32869
	Solvent	876
B-factors [Å^2]		
	Protein	42.13
	Solvent	52.34
R.m.s. deviations		
	Bond lengths [Å]	0.010
	Bond angles [°]	1.194
Ramachandran plot		
	Most favored [%]	97.2
	Additional allowed [%]	2.8

[a] Values in parentheses are for the highest resolution shell.
[b] $R_{merge}=\sum_h\sum_l|I(h)_l-\langle I(h)\rangle| / \sum_h\sum_l I(h)_l$, in which $I(h)_l$ is the l th observation of the reflection h and $\langle I(h)\rangle$ is the weighted average intensity for all observations l of reflection h.
[c] $R_{work}=\sum_h||F_{obs}(h)|-|F_{cal}(h)|| / \sum_h|F_{obs}(h)|$, in which $F_{obs}(h)$ and $F_{cal}(h)$ are the observed and calculated structure factors for reflection h respectively.
[d] R_{free} was calculated as R_{work} based on the 5% of reflections for the complex which were selected randomly and omitted from refinement.

Supplemental Figures 1-6

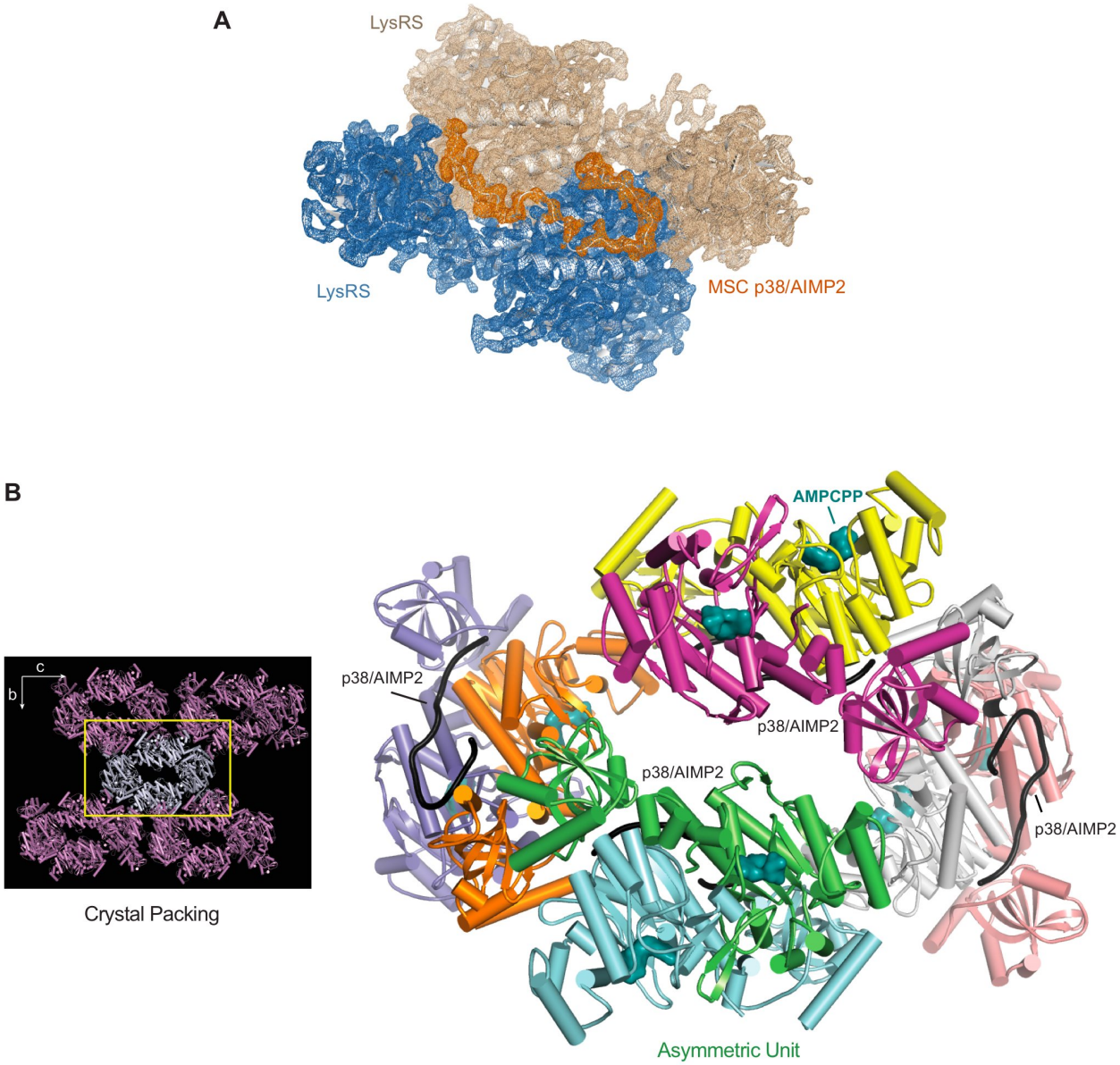

Figure S1

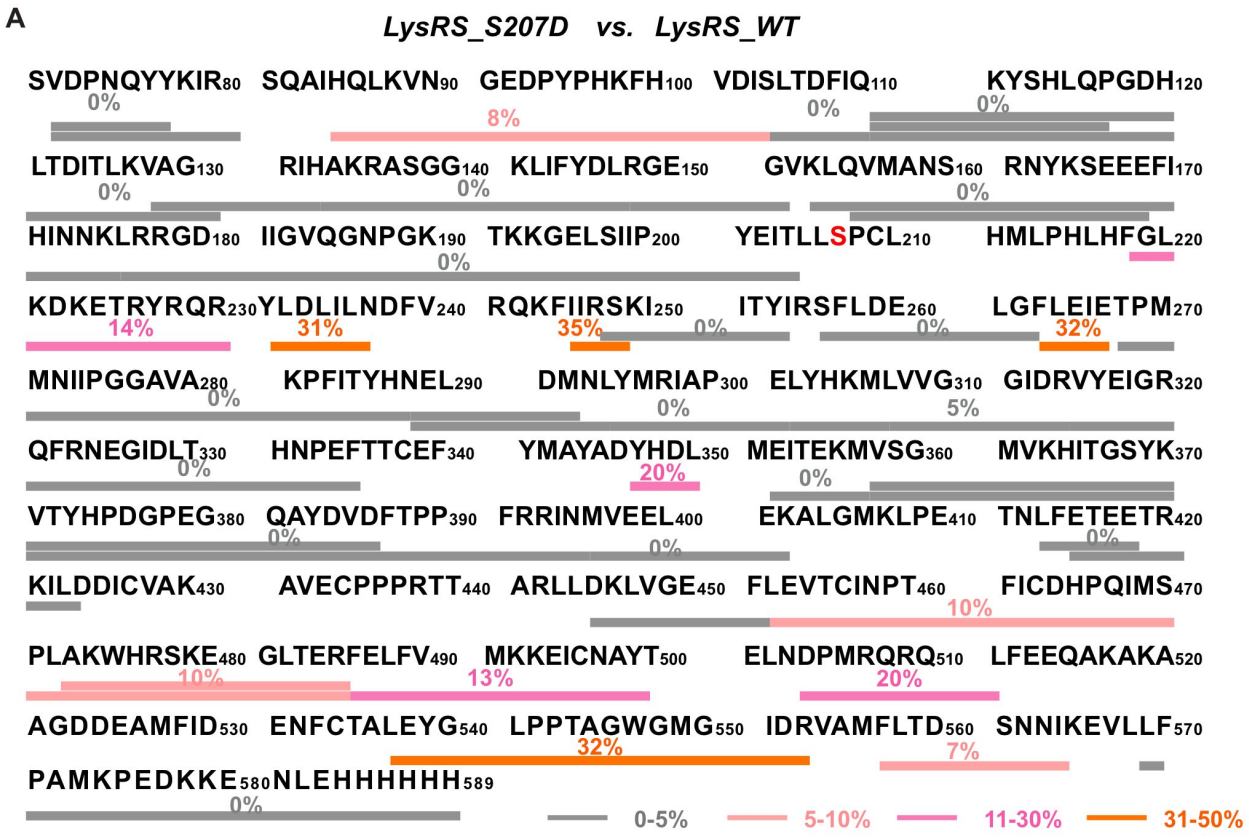
A
LysRS_S207D vs. LysRS_WT
SVDPNQYYKIR80 SQAIHQLKVN90 GEDPYPHKFH100 VDISLTDFIQ110 KYSHLQPGDH120
0% 8% 0% 0%
LTDITLKVAG130 RIHAKRASGG140 KLIFYDLRGE150 GVKLQVMANS160 RNYKSEEEFI170
0% 0% 0%
HINNKLRRGD180 IIGVQGNPGK190 TKKGELSIIP200 YEITLLSPCL210 HMLPHLHFGL220
0%
KDKETRYRQR230 YLDLILNDFV240 RQKFIIRSKI250 ITYIRSFLDE260 LGFLEIETPM270
14% 31% 35% 0% 0% 32%
MNIIPGGAVA280 KPFITYHNEL290 DMNLYMRIAP300 ELYHKMLVVG310 GIDRVYEIGR320
0% 0% 5%
QFRNEGIDLT330 HNPEFTTCEF340 YMAYADYHDL350 MEITEKMVSG360 MVKHITGSYK370
0% 20% 0%
VTYHPDGPEG380 QAYDVDFTPP390 FRRINMVEEL400 EKALGMKLPE410 TNLFETEETR420
0% 0% 0%
KILDDICVAK430 AVECPPPRTT440 ARLLDKLVGE450 FLEVTCINPT460 FICDHPQIMS470
10%
PLAKWHRSKE480 GLTERFELFV490 MKKEICNAYT500 ELNDPMRQRQ510 LFEEQAKAKA520
10% 13% 20%
AGDDEAMFID530 ENFCTALEYG540 LPPTAGWGMG550 IDRVAMFLTD560 SNNIKEVLLF570
32% 7%
PAMKPEDKKE580 NLEHHHHHH589
0%
0-5%
5-10%
11-30%
31-50%
B
Deuterium Uptake
AA231-236
S207D has 31% more deuterium uptake than WT
AA244-247
S207D has 35% more deuterium uptake than WT
AA537-553
S207D has 32% more deuterium uptake than WT
AA486-499
S207D has 13% more deuterium uptake than WT
AA504-511
S207D has 20% more deuterium uptake than WT
AA109-120
S207D has similar deuterium uptake as WT
AA357-386
S207D has similar deuterium uptake as WT
AA570-589
S207D has similar deuterium uptake as WT
Time (h)
LysRS_S207D
LysRS_WT

Figure S2

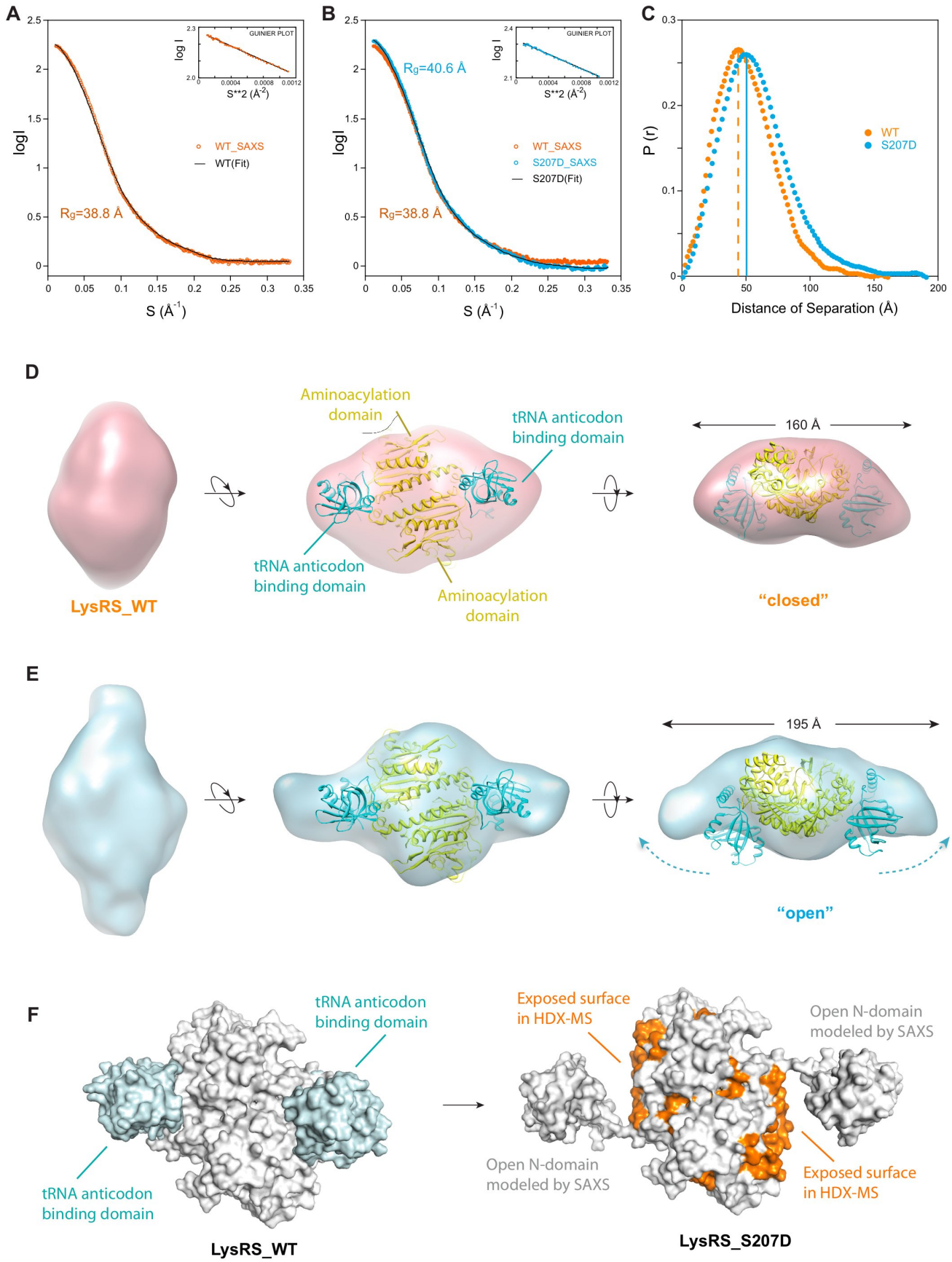
A
log I
S (Å^{-1})
GUINIER PLOT
log I
S**2 (Å^{-2})
WT_SAXS
WT(Fit)
Rg=38.8 Å
B
log I
S (Å^{-1})
Rg=40.6 Å
GUINIER PLOT
log I
S**2 (Å^{-2})
WT_SAXS
S207D_SAXS
S207D(Fit)
Rg=38.8 Å
C
P (r)
Distance of Separation (Å)
WT
S207D
D
Aminoacylation domain
tRNA anticodon binding domain
160 Å
tRNA anticodon binding domain
Aminoacylation domain
LysRS_WT
"closed"
E
195 Å
"open"
F
tRNA anticodon binding domain
tRNA anticodon binding domain
LysRS_WT
Exposed surface in HDX-MS
Open N-domain modeled by SAXS
Open N-domain modeled by SAXS
Exposed surface in HDX-MS
LysRS_S207D

Figure S3

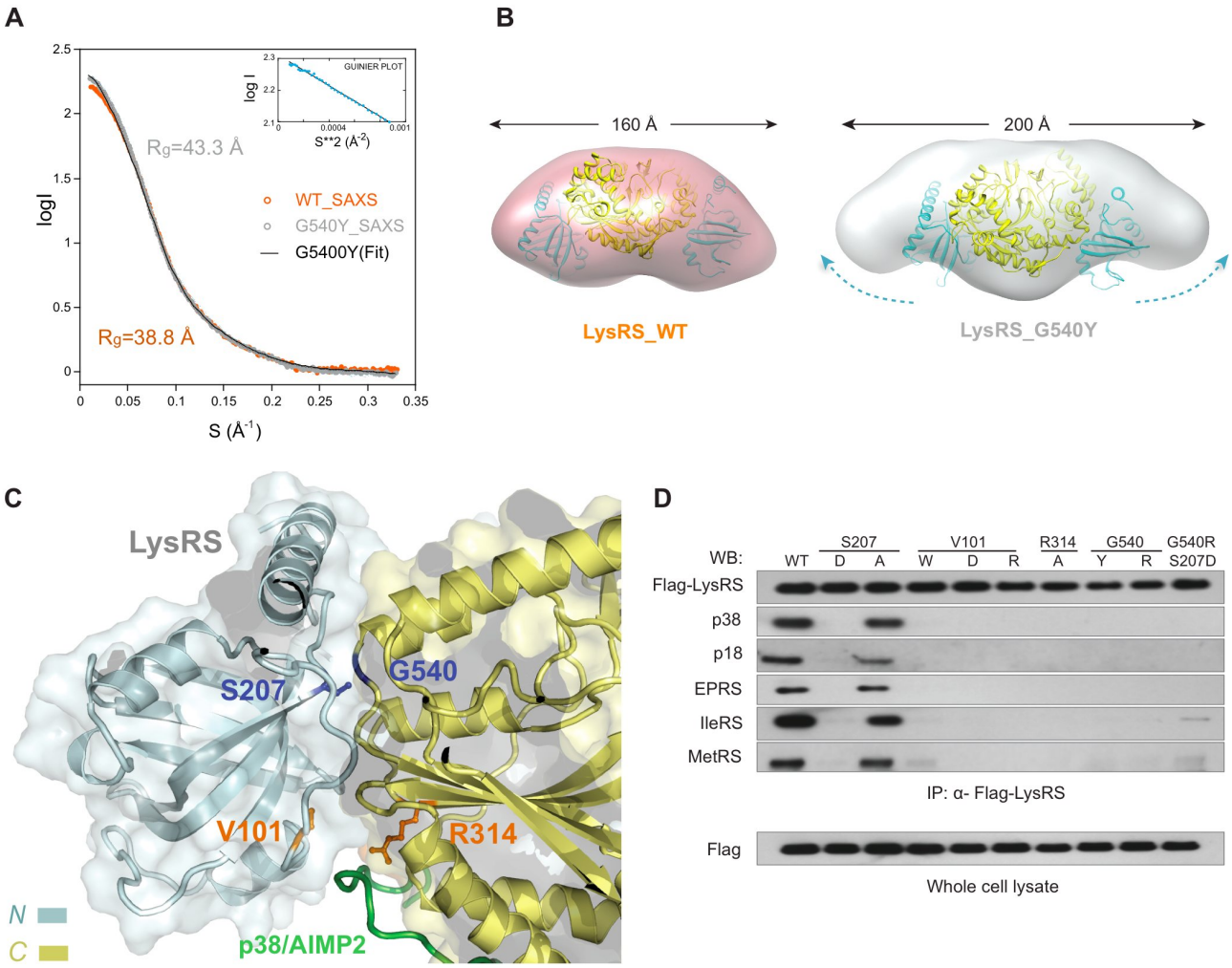
A
GUINIER PLOT
log I
S**2 (Å-2)
Rg=43.3 Å
WT_SAXS
G540Y_SAXS
G5400Y(Fit)
Rg=38.8 Å
logI
S (Å-1)
B
160 Å
200 Å
LysRS_WT
LysRS_G540Y
C
LysRS
S207
G540
V101
R314
p38/AIMP2
N
C
D
WB:
WT
S207
D
A
V101
W
D
R
R314
A
G540
Y
R
G540R
S207D
Flag-LysRS
p38
p18
EPRS
IleRS
MetRS
IP: α- Flag-LysRS
Flag
Whole cell lysate
E
Nucleus
LysRS
MITF
merged
Quiescent
Activated

Figure S4

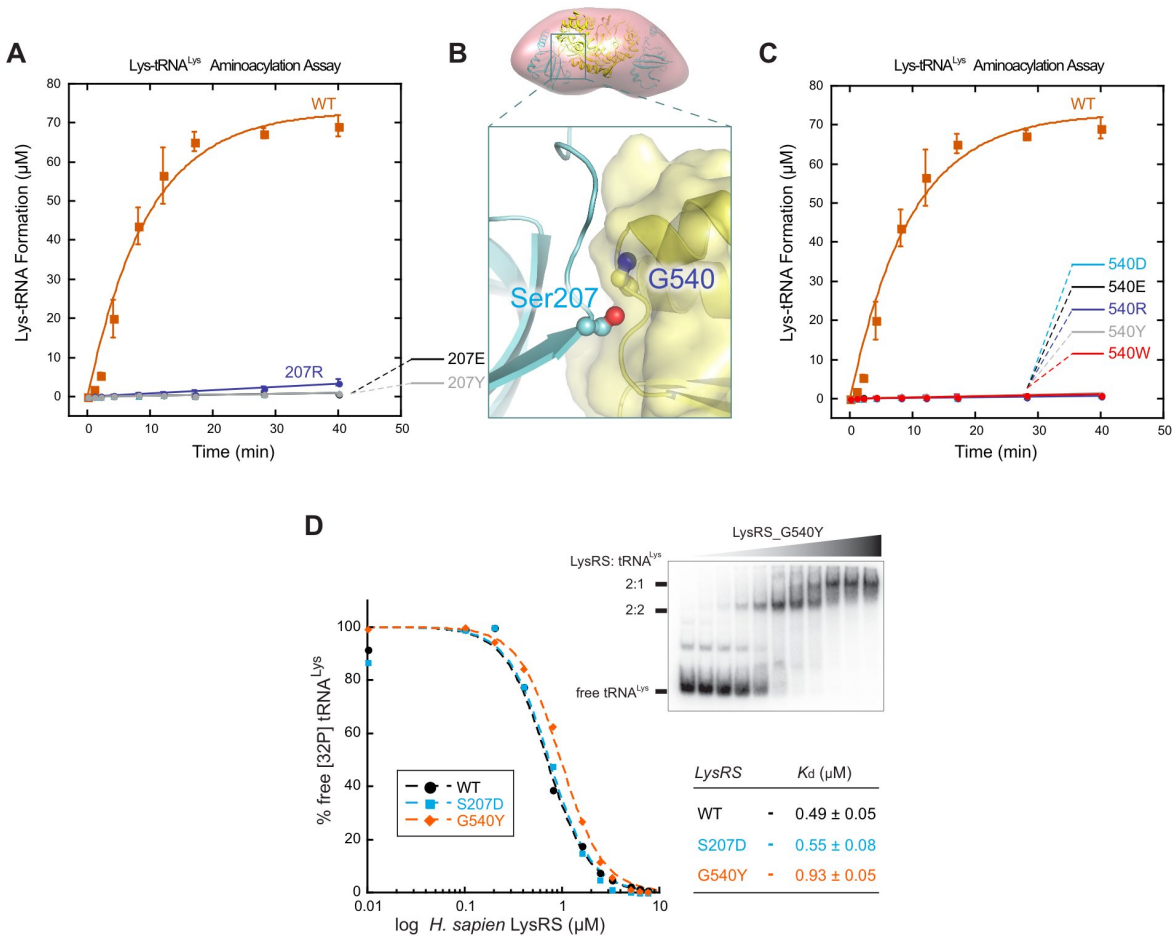
A
Lys-tRNA^Lys Aminoacylation Assay
Lys-tRNA Formation (μM)
Time (min)
WT
207R
207E
207Y
B
Ser207
G540
C
Lys-tRNA^Lys Aminoacylation Assay
Lys-tRNA Formation (μM)
Time (min)
WT
540D
540E
540R
540Y
540W
D
LysRS_G540Y
LysRS: tRNA^Lys
2:1
2:2
free tRNA^Lys
% free [32P] tRNA^Lys
log H. sapien LysRS (μM)
WT
S207D
G540Y
LysRS
Kd (μM)
WT - 0.49 ± 0.05
S207D - 0.55 ± 0.08
G540Y - 0.93 ± 0.05

Figure S5

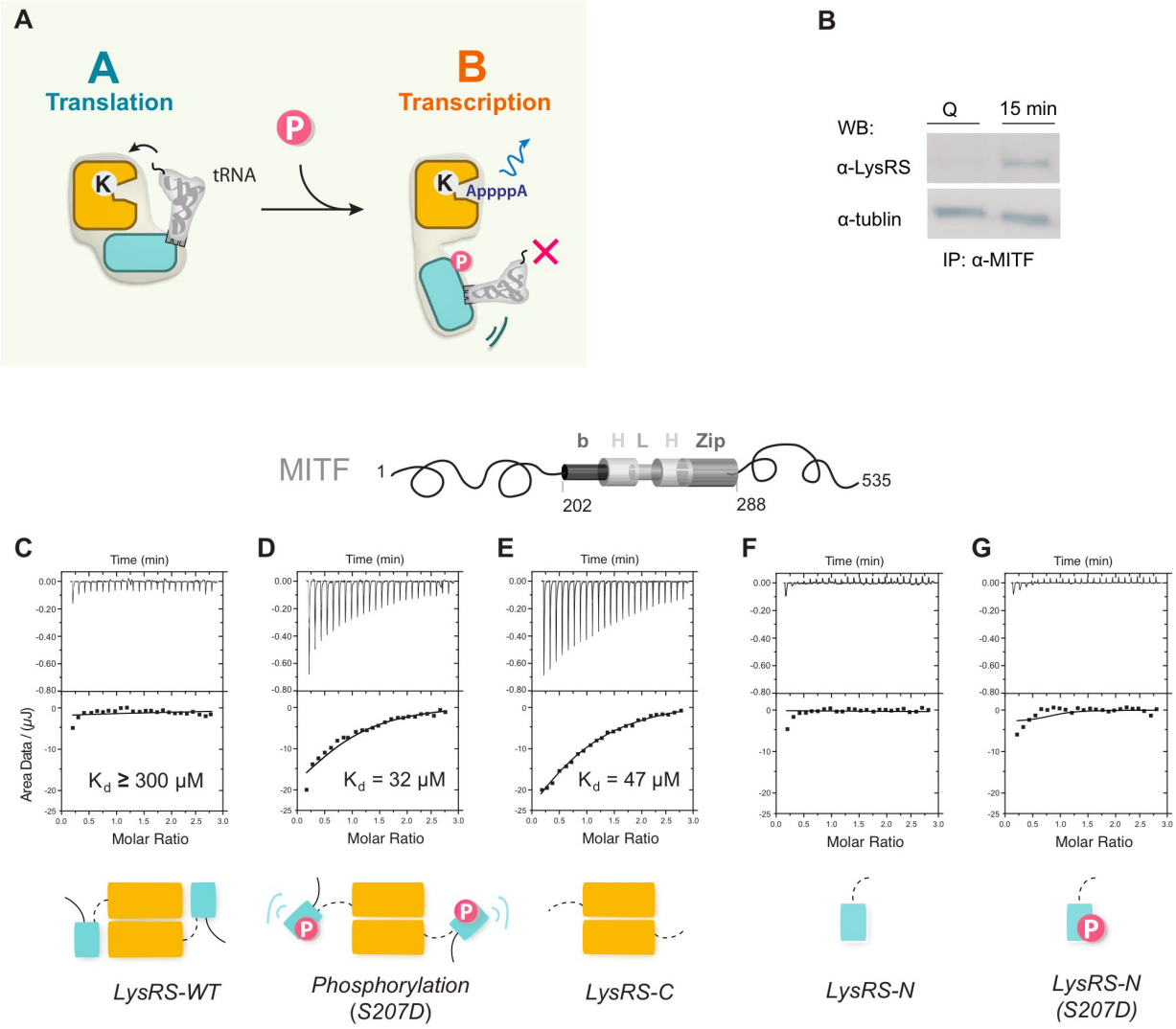
A
A
Translation
B
Transcription
tRNA
AppppA
B
Q
15 min
WB:
α-LysRS
α-tublin
IP: α-MITF
MITF
b
H
L
H
Zip
1
535
202
288
C
D
E
F
G
Time (min)
Area Data / (μJ)
Molar Ratio
K_d ≥ 300 μM
K_d = 32 μM
K_d = 47 μM
LysRS-WT
Phosphorylation
(S207D)
LysRS-C
LysRS-N
LysRS-N
(S207D)

Figure S6